International Journal of Rock Mechanics & Mining Sciences 145 (2021) 104839

Contents lists available at ScienceDirect

International Journal of Rock Mechanics and Mining Sciences

journal homepage: www.elsevier.com/locate/ijrmms

A deep learning approach for rock fragmentation analysis

Thomas Bamford [a], Kamran Esmaeili [a,*], Angela P. Schoellig [b]

[a] Department of Civil & Mineral Engineering, University of Toronto, 35 St. George St, Toronto, Ontario, M5S1A4, Canada
[b] Institute for Aerospace Studies, University of Toronto, 4925 Dufferin St, North York, Ontario, M3H5T6, Canada

ARTICLE INFO

Keywords:
Blasting
Rock fragmentation
Deep learning
DNN

ABSTRACT

In mining operations, blast-induced rock fragmentation affects the productivity and efficiency of downstream operations including digging, hauling, crushing, and grinding. Continuous measurement of rock fragmentation is essential for optimizing blast design. Current methods of rock fragmentation analysis rely on either physical screening of blasted rock material or image analysis of the blasted muckpiles; both are time consuming. This study aims to present and evaluate the measurement of rock fragmentation using deep learning strategies. A deep neural network (DNN) architecture was used to predict characteristic sizes of rock fragments from a 2D image of a muckpile. The data set used for training the DNN model is composed of 61,853 labelled images of blasted rock fragments. An exclusive data set of 1,263 labelled images were used to test the DNN model. The percent error for coarse characteristic size prediction ranges within ±25% when evaluated using the test set. Model validation on orthomosaics for two muckpiles shows that the deep learning method achieves a good accuracy (lower mean percent error) compared to manual image labelling. Validation on screened piles shows that the DNN model prediction is similar to manual labelling accuracy when compared with sieving analysis.

1. Introduction

The main objective of blasting in mines is to break in-situ rock mass to smaller rock fragments. More specifically, the goal is to achieve a specific fragment size distribution that eases handling, while minimizing damage to the final pit wall.[1] Fragmentation can affect the productivity and efficiency of downstream operations including digging, crushing, and grinding. To manage downstream effects, blast designs can be optimized through monitoring, analysis and modelling. Optimizing for cost, there are a range of close-to-optimal blast designs, but good blast design should adapt to the different rock mass conditions encountered at a mine site.[2,3]

Fragmentation as one of the important blast outcomes has been the focus of numerous studies because it plays an important role in creating downstream benefits during blasting. Both prediction and measurement of rock fragmentation have been used as a basis for blast optimization. To model the effect of rock mass condition and blast design on fragmentation, many empirical models have been developed. Notable fragmentation models include the Kuznetsov,[4] Kuz–Ram,[5] extended Kuz–Ram,[6] KCO,[7] and x_p-frag[8] models. More recently, fragmentation prediction has been reviewed in detail by Ouchterlony and Sanchidrián.[9]. The focus of fragmentation prediction includes characteristic sizes such as: x_{50} (median, 50% weight passing), x_{80}, x_{20} and x_{max} (maximum size), uniformity factor (n) for the Rosin–Rammler distribution, and curve-undulation parameter (b) for the Swebrec function. The x_p-frag model proposed by Ouchterlony et al.[8] emphasizes being distribution-free and only predicts characteristic sizes (x_p) so that the limitations of being fit to a specific distribution are reduced. Regardless of the model used, predicted parameters are commonly used to describe rock fragmentation with respect to fines generation, mid-range sizes, and oversize fraction. These studies acknowledge that predicted parameters will conform with trends, not absolute measures. To obtain evidence of an optimized blast, actual measurement is required.

Numerous techniques have been developed to measure fragmentation. Common methods include: qualitative visual observation, sieving, digital image analysis, and equipment monitoring. Visual observation and equipment monitoring methods provide inaccurate, qualitative and imprecise results. In the case of sieving, results are accurate but it is expensive and time-consuming. While digital image analysis methods have their own limitations, they have emerged as a common technique to measure fragmentation.[10] Many image analysis approaches have been developed using different sensors and data processing techniques to estimate the rock size distribution of a captured rock pile surface. These include photography,[11] stereo photography,[11] and laser scanning.[12] Raina[13] suggests that these methods can be grouped together as digital image analysis methods because they share similar limitations.

Major treatises have been published by the research community to describe digital image analysis methods and their limitations, namely

* Corresponding author.
E-mail addresses: thomas.bamford@mail.utoronto.ca (T. Bamford), kamran.esmaeili@utoronto.ca (K. Esmaeili), schoellig@utias.utoronto.ca (A.P. Schoellig).

https://doi.org/10.1016/j.ijrmms.2021.104839
Received 1 June 2020; Received in revised form 18 June 2021; Accepted 20 June 2021
Available online 25 June 2021
1365-1609/

those by Franklin and Katsabanis[14] and Sanchidrián and Singh.[15] Sanchidrián et al.[10] suggests that image analysis techniques generally share four main sources of error: only sampling a surface to estimate internal characteristics, image quality, delineation of fragments, and estimation of fines. The most persistent limitation is poor/wrong rock segmentation which can result in disintegration and fusion of rock fragments.[16] Due to this, extensive manual editing is usually required to correctly delineate fragments in captured rock images, a process that is time-intensive. As Ramezani et al.[17] noted, the main challenge in rock segmentation is being robust when there are variations in lighting, image contrast, and complex rock texture and shape. The studies using stereo photogrammetry[11,18] and laser scanning[19] present techniques to improve automated rock segmentation. While these techniques have improved rock segmentation, a number of other limitations still remain. For example, Sanchidrián et al.[10] and Thurley[19] both find that fines estimation still remains a major source of error in image analysis. To reduce this error when measuring muckpile fragmentation, Ouchterlony and Sanchidrián[9] splices results from digital image analysis (+10 cm) or in-pit sorting (+2.5 cm) with laboratory sieving results. However, implementing sieve sampling or in-pit sorting methods are expensive and can disrupt production.

To increase the measurement frequency, area covered, and resolution of fragmentation measurement for muckpiles, Unmanned Aerial System (UAS) photography has been proposed by a number of studies.[20–23] Through frequent data collection by UAS methods, the statistical reliability of the fragmentation measurement can be improved, as more samples are collected to understand population characteristics. However, these benefits are significantly hindered because poor/wrong automated rock segmentation has to be corrected through extensive manual editing. Ramezani et al.[17] and Schenk et al.[24] used deep neural networks (DNNs) as a first step in fragment segmentation to improve automated delineation. Their methods and results are discussed in more detail in Section 2. The results from Ramezani et al.[17] and Schenk et al.[24] have enabled fast and automated measurement but their strategy requires further investigation to better understand the accuracy and limitations of using DNNs for fragmentation measurement. Also, it should be noted that any limitations presented by data used to train DNNs are transferred to their results. For example, a DNN trained using 2D images will only be able to sample the surface of the pile.

This study presents the results of using deep learning strategies for rock fragmentation analysis. A convolution neural network architecture has been trained to predict scaled characteristic sizes of blasted rock fragments directly from a 2D image using an end-to-end deep learning strategy. The study evaluates the accuracy and performance of the DNN model as a tool for automated and fast rock fragmentation analysis. The outcomes of this evaluation demonstrate ±25% percent error for coarse size prediction on the test set where 50% of the test set has a percent error of ±10%. Validation of the DNN model on sieved piles shows accurate prediction compared to manual image labelling.

2. Fragmentation and deep learning

Ramezani et al.[17] proposed using a DNN, a form of an artificial neural network (ANN), prior to watershed segmentation to improve automated delineation. Their network used a pixel classifier that uses a square patch of raw pixels to predict if an image pixel in the patch centre is an edge, rock, or fines. The network is trained using images captured primarily by cameras targeting shovel buckets, which can limit image resolution of the rock pile.[11] The prediction is then refined using watershed segmentation to close edges. When tested using 64 images, Ramezani et al.[17] reported that their pixel error was 4.09 ± 1.4%. It was not clear how many images were included in their training data set. Ramezani et al.[17] also compared the results of their DNN technique with sieving. Only 2 measurements were compared but the DNN automatic segmentation produced results that were within 10% of the sieving measurements. Their results are promising but require further investigation to better understand their method's accuracy and limitations.

Schenk et al.[24] applied Mask R-CNN, developed by He et al.,[25] to rock segmentation. Their network used feature extraction over the whole image, followed by bounding box recognition to predict the existence of fragments and their masks to define size and shape. Only fragment and background classes are predicted by the network. The network was initialized on Mask R-CNN weights trained on the MS COCO data set[26] and fine-tuned using images from a laboratory setup. A total of 4323 laboratory images with a size of 1024 × 1024 were used to label approximately 1000 mid-size to coarse fragments (greater than 10 mm) over 4 different rock pile configurations. The labelling of only mid-size to coarse fragments extremely limited the method's ability to estimate fines. Their data was augmented for training using 50% overlap between images, mirroring, rotating, cropping and up/down scaling. Only 8 laboratory validation results were reported by Schenk et al.[24] for correct prediction of the median size range, x_{50}, as measured through sieving. The performance of predicting other fragmentation parameters, such as x_{80} or n, was not considered. An average absolute percent error of 59% and 33% for x_{50} size prediction was calculated by the authors of this study using presented data for single-scale and multi-scale equivalent circle methods, respectively. This range of percent error is high but expected because they have compared the results of 2D image analysis with sieving measurements. Schenk et al.[24] also presented qualitative results of applying their network to muckpile images captured by UAS methods in the field. While these qualitative results indicate the quality of coarse fragment segmentation, they do not provide the performance of their method when predicting other fragmentation parameters, such as the median size, x_{80}, or n. Their results are encouraging but as Schenk et al.[24] indicated, more data acquisition and annotation is required to improve their results.

3. Proposed deep learning approach

An early version of the DNN model used a pixel classifier to segment rocks; however, the results were not satisfactory. This was attributed to only having a small data set of 1200 sample images available at the time it was trained. Fig. 1 shows a comparison of the manually labelled and pixel classifier image results. While major regions were identified, rock edges were poorly defined or absent when the pixel classifier was used. To achieve accurate measurement, post-processing and manual editing would have been required to define rock edges. To improve the performance of the DNN model, this study explored an end-to-end deep learning strategy.

The fragmentation parameters measured using size analysis are directly predicted by the DNN model in this study. Size analysis parameters include characteristic sizes x_{20}, x_{50}, x_{80}, and x_{max}. These fragmentation parameters were chosen as important features for the labelled images in the data set due to their importance in fragmentation prediction models.[10] Using these parameters, it is possible to make a comparison between the predicted and measured fragmentation. As shown in Fig. 2, the input to the proposed DNN model is a 2D image and the output are the four measured characteristic sizes x_{20}, x_{50}, x_{80}, and x_{max}. The details of the DNN model architecture illustrated in Fig. 2 are described in Section 5. As noted in Section 1, this deep learning approach will still be limited by the data used to train the proposed DNN model. For example, the DNN model will only be able to sample the surface of the pile because the input data is a 2D image.

4. Data set

Deep learning strategies work best when training is based on a large representative data set. This allows DNNs to generalize to differing conditions such as lighting, scale, rock type, fragmentation, rock texture and environment. The data set used for training and testing the DNN model is composed of 2D images that have been manually analysed and

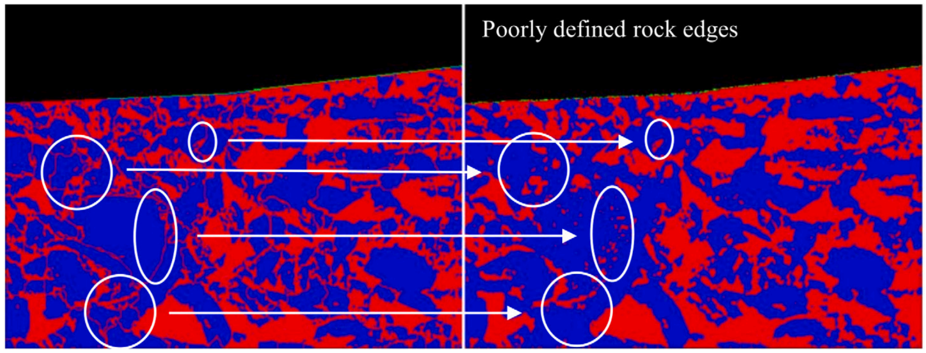

Fig. 1. Manually labelled image (**left**) and pixel classifier output (**right**) from early version of the DNN model. Rock faces and edges are represented by blue and red, respectively. As seen in the pixel classifier output (**right**), rock edges are poorly defined or missing when compared with the manually labelled image (**left**). (For interpretation of the references to colour in this figure legend, the reader is referred to the web version of this article.)

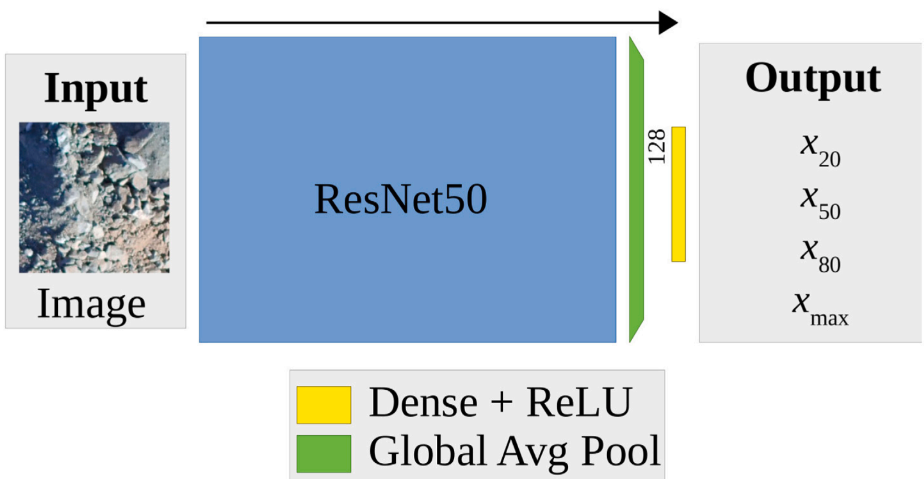

Fig. 2. DNN model architecture illustration. The ResNet50 base model is followed by global average pooling and a dense layer with 128 nodes before the fully connected output layer.

labelled using Split-Desktop by Split Engineering LLC.,[27] a commercial image analysis software for fragmentation measurement. The images are labelled to indicate regions of rock, edge, fines, and background. Background represents areas that do not contain the analysed rock pile. Fig. 3 presents an example of raw and labelled source image. The data is composed of image sets of muckpiles in varying lighting, scale, rock type, fragmentation, and perspective taken in open pit mines and quarries. Table 1 provides a summary of the image sets currently used for training and testing the DNN model. As indicated in Table 1, there are a total of 443 source images in our current image sets. Note that these image sets had different perspectives: terrestrial and aerial. Ideally, the training data should have the same perspective and quality as the final application. The initial application during DNN model development was to measure fragmentation using data collected from the aerial perspective. However, this type of data was limited, thus, ground-based images were used as the main source of training data. This was found to influence the DNN model when testing performance using aerial-based images as described in Section 7.1. Once more data is available, future work should focus on training DNN models using data collected with the same perspective and quality.

To generate samples with uniform size, patches were extracted from the labelled images from each image set. The grids in Fig. 3 illustrate the patches extracted from the source image. The developed deep learning code is able to use any image size; however, once a neural network is trained at a certain input size, this size is fixed for that network. A size of 512 × 512 pixels was chosen for this study because it was found to have enough coverage to identify oversize rock fragments and variations in fragmentation within the source images. With a uniform size of 512 × 512 and without patch overlap, patch extraction produced 3301 sample images. These sample images contain a total of 1,348,440 measured fragments.

Table 1
Image sets used to create train and test data sets for the DNN model.

Image set name	Source images	Patches extracted (No overlap)	Perspective	Analysis
2017	10	60	Aerial	Split-Desktop
2018	430	2743	Terrestrial	Split-Desktop
2019 Orthomosaics	3	498	Aerial	Photo editor
Total	**443**	**3301**		

While this is a large number of images, more samples are required to produce the best deep learning results. One method of adding more sample images would be collecting and labelling more source images; however, this would require significant expense and time. Another method of adding more sample images is data augmentation. To augment the data, an overlap and rotation method was used when extracting patches. With an overlap of 128 pixels, 63,116 sample images were produced. These sample images contain a total of 23,125,486 measured fragments. Increasing to this sample size, created significant improvements when iterating to find the best DNN weights and resulting performance.

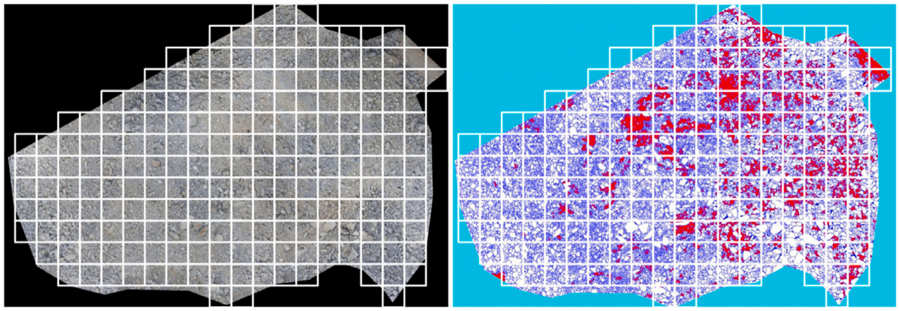

Fig. 3. Source image of Muckpile 1 (**left**) with its labelled image (**right**). Rock edges, fines, and background are represented by blue, red, and cyan, respectively. The white grid shows 512 × 512 sample images extracted using patch extraction with 0 px overlap. (For interpretation of the references to colour in this figure legend, the reader is referred to the web version of this article.)

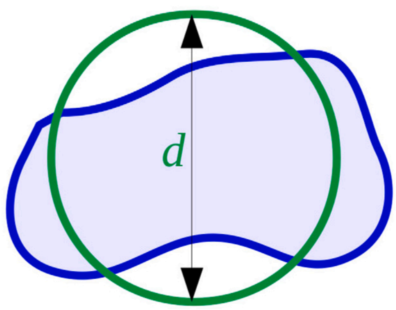

$$d = 2\sqrt{\frac{A}{\pi}} \qquad V = \frac{4}{3}\pi\left(\sqrt{\frac{A}{\pi}}\right)^3$$

Fig. 4. Fragment size, d, as the equivalent diameter of the fragment's area, A. Volume, V, is the equivalent spherical volume of A.

In this study, a fragmentation parameter, such as x_{50}, is directly predicted from an input image by the DNN. As described in Section 3, four characteristic sizes were chosen as features for the DNN model to measure due to their prominence in fragmentation prediction models. To achieve this, each sample label image has to be analysed to measure each parameter. An analysis code was written to measure various fragmentation parameters from a manually labelled image. The analysis code first creates a mask for the labelled rock faces using a predefined colour in the manually labelled image. Then the properties of the rock regions in the mask are measured to calculate equivalent size, area and volume. Equivalent size, area and volume are then combined with measurements of the manually labelled rock edges and fines areas to perform an area analysis and size analysis based on Cunningham[28] and Maerz et al.,[29] respectively. The result of these analyses are the fragmentation parameters listed in Table 2.

This study defines fragment size as the equivalent diameter of the fragment's area as illustrated in Fig. 4. Fines are defined as having a fragment size less than 3 px. This definition of fines is based on image pixels so that the DNN model does not predict image scale. As such, the fines definition varies according to image scale, not physical fragment size. Oversize fragments are defined as having a fragment size greater than 20% of the image width, or 102 px. This oversize definition was made so that oversize fragments are greater than 1 m in size when images are captured with a ground sampling distance (GSD) of 1 cm/px.

Once the fragmentation parameters were measured using the labelled images, they were randomly shuffled and split into three subsets. This splits the data set into 61,853 samples for training, 631 for validation, and 632 for testing. These subsets were generated prior to DNN model exploration and were not regenerated during training and testing. In addition to the images used in the validation and testing data sets, Section 7 presents the result of additional testing in which an exclusive set of orthomosaics (250 samples) and screening image (8 samples) data were used for testing the accuracy of the model. These images were not employed during training. Fig. 5 presents histograms for each fragmentation parameter included in the training and testing (validation and test) data sets. These histograms show that the training and testing data sets have similar distributions for each fragmentation parameter. Note that the units in this study are based on image pixels because image scale is applied in post-processing. The validation set was used when exploring training hyperparameters and trying different architectures to avoid over-fitting to the test set. The results presented in Section 6 are calculated using only the test set. To improve training, each fragmentation parameter is scaled from 0 to 1 using the minimum and maximum value of each parameter within the data set. The scaling transformation was saved so that DNN predictions could be rescaled back to the original parameter's range. All the figures show DNN outputs after they have been rescaled.

5. Model architecture and training

A convolutional neural network (CNN) is a DNN class that is commonly applied to analysing images. In this study, a CNN with ResNet50[30] as a base and global average pooling followed by dense fully connected layers as the top was constructed to predict fragmentation parameters from an input image. The ResNet50 base architecture is composed of 50 layers, including 49 convolution layers and one dense layer. This base architecture also has one max pooling and one global average pooling layer which do not have trainable weights. Batch normalization and the rectified linear unit (ReLU) activation function was applied after every convolution layer. In Table 3, each square bracket in the first column represents a bottleneck residual block, and every row in the brackets represents one layer of operation. The inner structure of a bottleneck residual block is described in He et al.[30] As found by He et al.,[30] the use of bottleneck residual blocks leads to an effective and computationally efficient training process of the base network.

DNNs are more commonly used in logistic regression to solve classification problems; however, since the parameters being predicted are in a continuous, rather than a discrete series, regression is used. To achieve this in the DNN architecture, the final fully connected layer uses a linear activation function before the output. The ReLU activation function is used in the hidden dense layer. This study only presents the most recent architecture; however, a large number of iterations through many different architectures was used to reach the results in Section 6. Early iterations attempted to predict parameters separately using the same architecture; however, this resulted in sub-optimal results when considering the total size of the models used. In this study, one model was used to predict all parameters for fragmentation size analysis. We propose that size analysis parameter prediction benefits

Table 2
Parameters measured by the analysis code. Area analysis and size analysis were based on the studies by Cunningham[28] and Maerz et al.,[29] respectively. The particle size, d, follows the definition in Fig. 4.

Area analysis	Size analysis
Surface area (not background)	Fragment count ($d > 3$ px)
Fragment area ($d > 3$ px)	Granulation histogram
Oversize count ($d >$ 20% image $\min[w, h]$)	Granulation curve (cumulative sum)
Size index (Fragment area / surface area)	% Passing sizes (x_{10}, x_{20}, …, x_{90}, x_{99})
Subsize index (100% - size index)	Average sphericity
% Optical fines (Edges, fines, $d < 3$ px)	Fragment size statistics (min, max, mean, median, mode, standard deviation)
% Mid-range sizes (3 px $< d <$ 20% image min)	Ros-Ram distribution (x_c, n)
% Oversize ($d >$ 20% image min)	Swebrec distribution (x_{max}, x_{50}, b)

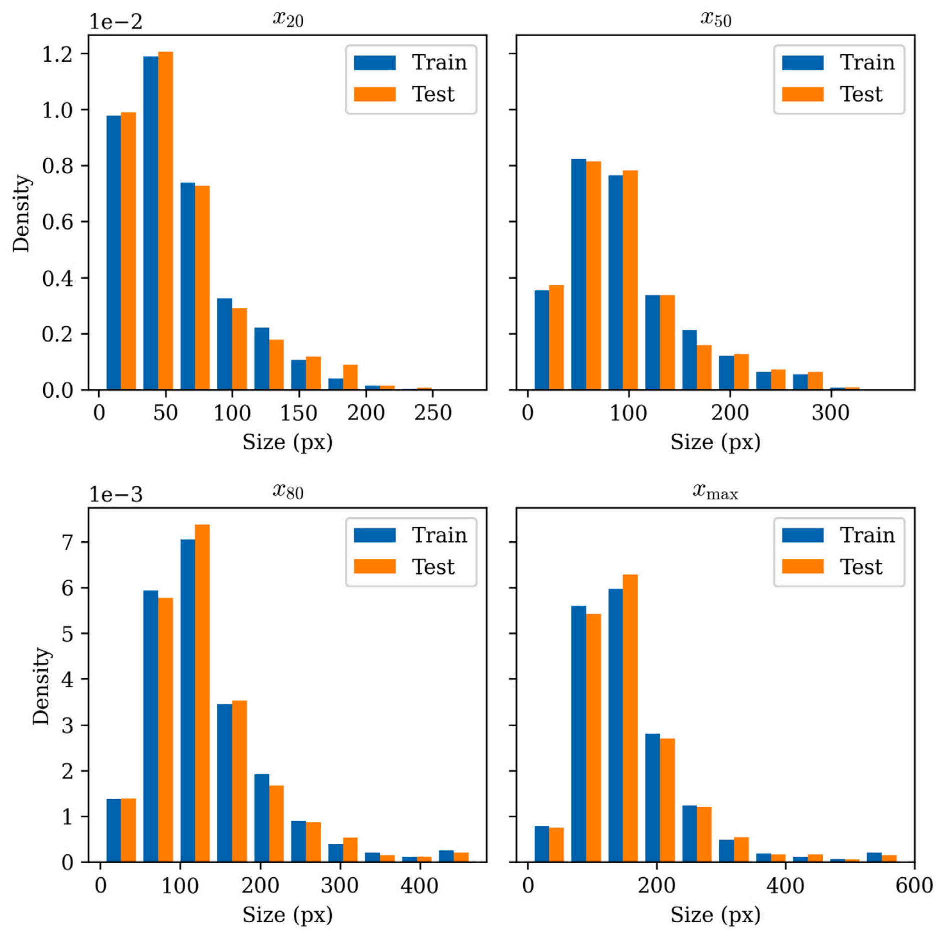

Fig. 5. Histograms of fragmentation parameters included in the training and testing (validation and test) data sets used to train and test the DNN model. The data sets contain 61,853 training samples and a total of 1263 validation and test samples.

from sharing information between parameters and thus benefits from multi-task learning applied using one model. The architecture used is illustrated and summarized in Fig. 2 and Table 3, respectively.

During training, base network weights were initialized to ResNet50 weights pre-trained on ImageNet. This was done to help avoid over-fitting to the training data set and was found to produce better performance than using random weight initialization.[31] Top network weights were initialized to random values. The training set described in Section 4 was used to provide input images and their measured outputs. The network predicted output was compared to the actual output parameter value and the mean squared error (MSE) was calculated. The Adam[32] minimization algorithm was applied to determine new values for network weights through backpropagation. Due to the size of the training set, batches of training data had to be used because the computer used for training did not have enough GPU memory. This was implemented using process-based threading so that a queue of batches could be loaded into memory using parallel CPU processes. The training process was implemented in the Keras Python deep learning library.[33] Table 4 provides the computer configuration and approximate computation time during training. The batch size, number of epochs (iterations on the training set), training loss (MSE for whole training set), and validation loss (MSE for validation set) calculated during training are provided in Table 5 for the DNN model. During training of the DNN model, training and validation loss for each epoch were monitored to stop training once model improvement slowed to avoid over-fitting the model to the training set. See Fig. 6 for the training and validation loss calculated after each epoch of training. As can be seen in Fig. 6, when the number of epochs reaches about 60, no significant improvement in training loss and validation loss is observed.

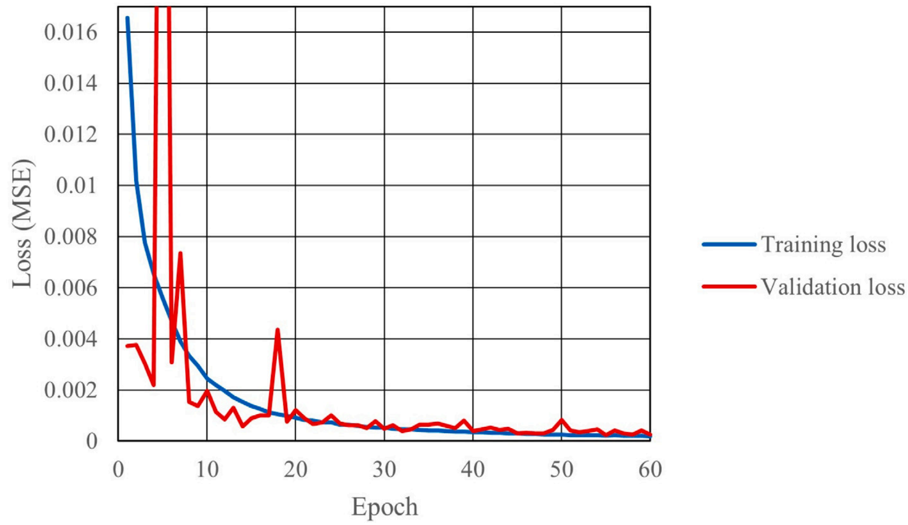

Fig. 6. Training and validation data set loss calculated after each epoch of training.

Table 3
DNN model architecture summary.

Layer (Operation)	Output shape
Input 1	512 × 512 × 3
Convolution (Conv) 1 (Conv 7 × 7, 64)	256 × 256 × 64
Max Pool 1 (Max pool 3 × 3)	128 × 128 × 64
Block 1_x $\begin{bmatrix} \text{Conv } 1\times 1, 64 \\ \text{Conv } 3\times 3, 64 \\ \text{Conv } 1\times 1, 256 \end{bmatrix}\times 3$	128 × 128 × 256
Block 2_x $\begin{bmatrix} \text{Conv } 1\times 1, 128 \\ \text{Conv } 3\times 3, 128 \\ \text{Conv } 1\times 1, 512 \end{bmatrix}\times 4$	64 × 64 × 512
Block 3_x $\begin{bmatrix} \text{Conv } 1\times 1, 256 \\ \text{Conv } 3\times 3, 256 \\ \text{Conv } 1\times 1, 1024 \end{bmatrix}\times 6$	32 × 32 × 1024
Block 4_x $\begin{bmatrix} \text{Conv } 1\times 1, 512 \\ \text{Conv } 3\times 3, 512 \\ \text{Conv } 1\times 1, 2048 \end{bmatrix}\times 3$	16 × 16 × 2048
Global Average Pooling 2	2048
Dense 1	128
Dense 2	5
Total parameters	**23,850,629**

Table 4
Computer configuration used during model training.

Specification	Configuration
Graphics processor (GPU)	Nvidia GeForce GTX 2080 Ti
GPU cores	4352
GPU total memory	11 GB
Computer processor (CPU)	Intel Core i9-7920X Skylake-X CPU at 2.9 GHz
CPU cores	12
Memory	64 GB
Computation time per epoch for training set described in Section 4 and the architecture summarized in Table 3.	2160 s

6. Test set

The test set described in Section 4 was used to evaluate the performance of the trained network. Table 5 presents the testing loss (MSE) for the DNN model. The percent error statistics are illustrated as box plots in Fig. 7. As shown in the figure, the percent error for x_{50}, x_{80} and x_{max} range within ±25%, where 50% of the test set has a percent error of ±10%. This range of error was considered acceptable because it is within the reported 30%–40% percent error found for coarse fragments when using digital image analysis for fragmentation measurement.[10] Although, depending on the application, this amount of error is considered acceptable; however, further improvement may be required if greater accuracy is needed. As expected, the percent error for x_{20} has a wider range from −70% to 20%. Note that a negative percent error indicates overestimation whereas positive indicates underestimation. This behaviour was expected because digital image analysis was found to produce less accurate results when measuring small fragment sizes.[10] As reported by Sanchidrián,[10] digital image analysis methods had a percent error of 80%–90% when measuring small fragments, so the error found for x_{20} is considered acceptable. To improve the DNN model's performance on the test set more data could be collected, other neural network architectures and hyperparameters could be searched, and regularization techniques could be used during training.

Table 5
Training parameters and results calculated for the DNN model. Human, training, validation, and test losses are MSEs for the human error, training, validation, and testing data sets, respectively.

Training	Size analysis
Epochs	60
Batch size	8
Human loss	0.008474
Training loss	0.000195
Validation loss	0.000262
Testing loss	0.000224

Fig. 8 presents residual plots throughout the range of predicted values. These plots show that residuals are symmetrically distributed, clustering toward the middle of the plot, and they are clustered around low values (±20 px). This was considered acceptable behaviour for the DNN model since no problematic pattern in residuals was observed.

While tuning the architecture and network training, image collections for the best and worst predictions were examined. This helped understand how the network performed for different types of image conditions and fragmentation. A collection of sample images for the best and worst fragmentation analysis predictions for the network trained in Section 5 are presented in Fig. 9 and Fig. 10, respectively. Fig. 9 illustrates that the best predictions for size analysis are made for images with well-defined rock boundaries and mid-range to coarse fragmentation. Fig. 10 shows that predictions are poor for images

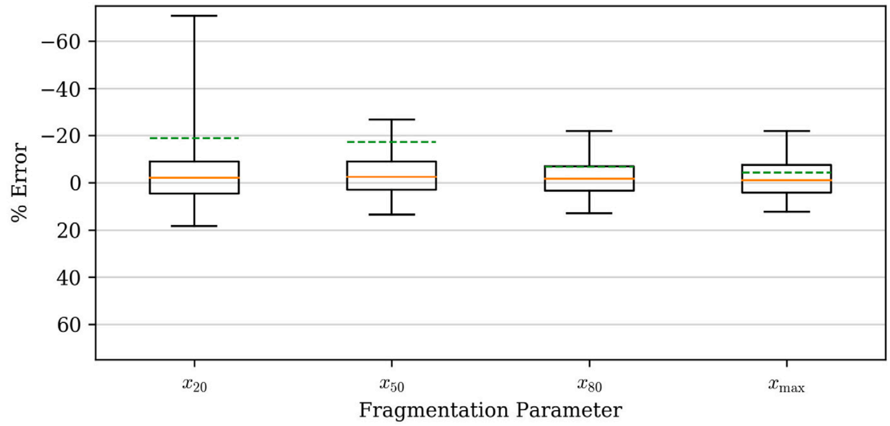

Fig. 7. Percent error box plots for fragmentation parameters predicted from the test set. Orange solid line and green dashed lines are median and mean, respectively. Whiskers are at the 5% and 95% percentiles. Outliers beyond the whisker range are not plotted.

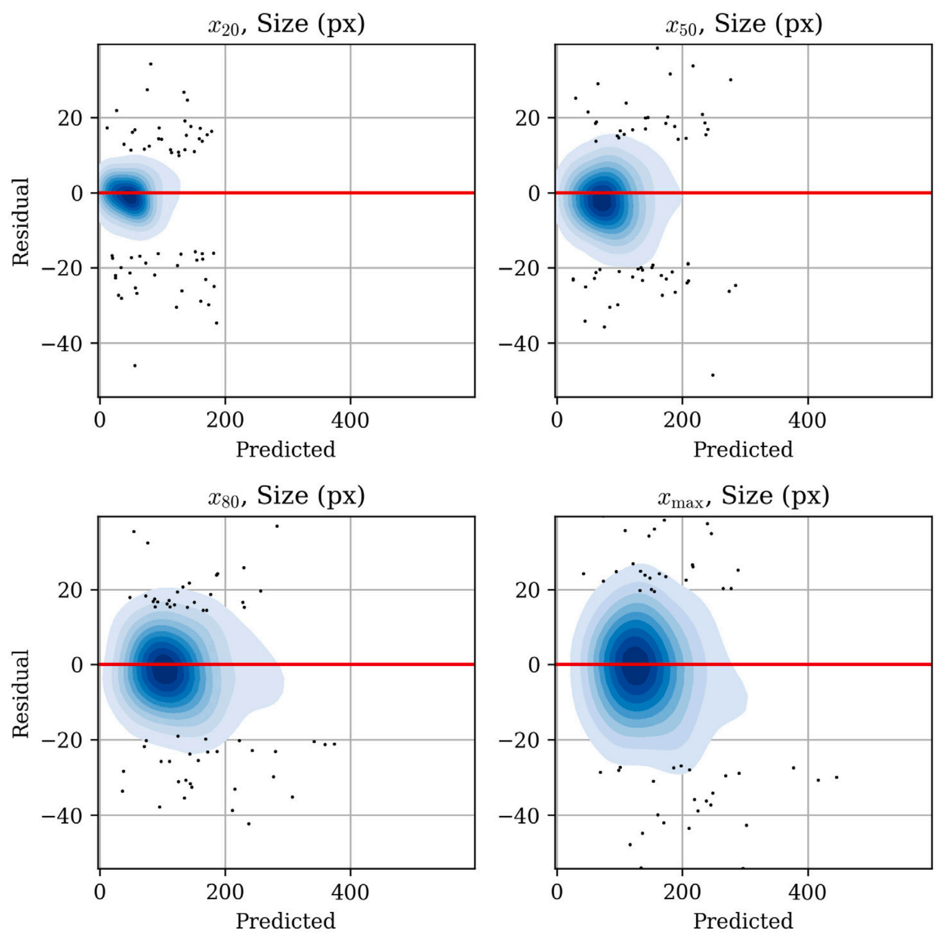

Fig. 8. Residual plots for each fragmentation parameter predicted. Blue contour plots represent density of predicted points. Black dots are outliers beyond the 5% and 95% residual percentiles. (For interpretation of the references to colour in this figure legend, the reader is referred to the web version of this article.)

containing more background and fine to very fine or oversize fragmentation. These results align with the findings of Sanchidrián et al.[10] that digital image analysis techniques perform well for coarse fragmentation and poor for fine fragmentation. An interesting finding when inspecting Fig. 9 and Fig. 10 is that scale objects are found in both collections. This indicates that the model may have trained to mask scale objects for various types of fragmentation.

7. Model validation

7.1. Comparison with labelled orthomosaics

To further validate the results in Section 6 with additional field data, two blasted muckpiles were manually labelled and compared with their predicted fragmentation parameters using the DNN model. Muckpile 1 and Muckpile 2 were the results of production blasts in quarries. An

Fig. 9. Collection of sample images for the best size analysis predictions.

orthomosaic was generated for each muckpile and manually labelled using a photo editor. These orthomosaics were not used during neural network training so that they could be used for model validation. These muckpiles were chosen because they show a range of different fragmentation.

Muckpile 1, shown in Fig. 1, had an orthomosaic labelled at a GSD of 5 cm/px. The orthomosaic was manually delineated by an expert and novice with 3 years and 3 months of experience with fragmentation image analysis, respectively. The expert and novice took 11.5 h and 13.5 h for manual labelling, respectively. To compare the expert and novice analyses, patch extraction and analysis code were used to generate 153 non-overlapping image samples at a GSD of 1 cm/px with their measured fragmentation parameters. The MSE loss between novice and expert analysis was calculated for size analyses parameters and is assumed to be the amount of human error present in image labelling. This human loss was used as a target when iterating through different models and architectures, assuming that the expert analysis has minimum error compared to novice analysis. However, further data labelling will be required to better understand human error since it is understood that even an expert does not produce perfect delineation. Table 5 provides the MSE loss between novice and expert analysis for size analysis parameters (human loss). For size analysis, the trained models performed better than the calculated human loss using the test set. Fig. 11 shows fragmentation parameter percent error calculated between novice and expert analysis (red box plots). For x_{20}, x_{50}, x_{80}, and x_{max} the mean percent error is −50.52%, −16.55%, −24.22%, and −20.65%, respectively. As this illustrates, novice analysis when compared with expert analysis is bias to overprediction of characteristic sizes. When comparing novice and expert labelling, the novice does not delineate fine particles whereas fines regions are delineated by the expert.

The generated image samples were then used as input to the predictive neural network to compute predicted parameters. The DNN took a total of 5 s to compute predicted parameters for all 153 image samples. Fig. 11 provides a comparison of model predictions with respect to the expert analysis using percent error box plots (blue box plots) for each fragmentation parameter. As Fig. 11 illustrates, DNN model predictions have an error range less than novice analysis when compared with expert analysis, except for x_{20}. For x_{20}, x_{50}, x_{80}, and x_{max} the mean percent error is −144.14%, 2.85%, 5.49%, and 3.40%, respectively. As this illustrates, the DNN model has a better mean percent error than the novice analysis, except for x_{20}. The error ranges for coarse and fine sizes are considered acceptable because the range is less than novice analysis and most predictions fall within the ranges reported for image analysis error by Sanchidrián et al.[10]. Fig. 11 also shows that the DNN model when compared with expert analysis is bias to underprediction of characteristic sizes, except for x_{20}. We propose that this is caused by data mismatch between the training data set and the orthomosaic for Muckpile 1. To reduce this error, more muckpile orthomosaics should be collected and labelled for inclusion during neural network training. When collecting this data, GSD should be kept constant or similar to ensure that the non-dimensional size ranges remain comparable to each other.

Muckpile 2, shown in Fig. 12, had an orthomosaic labelled at a GSD of 1.5 cm/px. This orthomosaic was manually labelled for 32.5

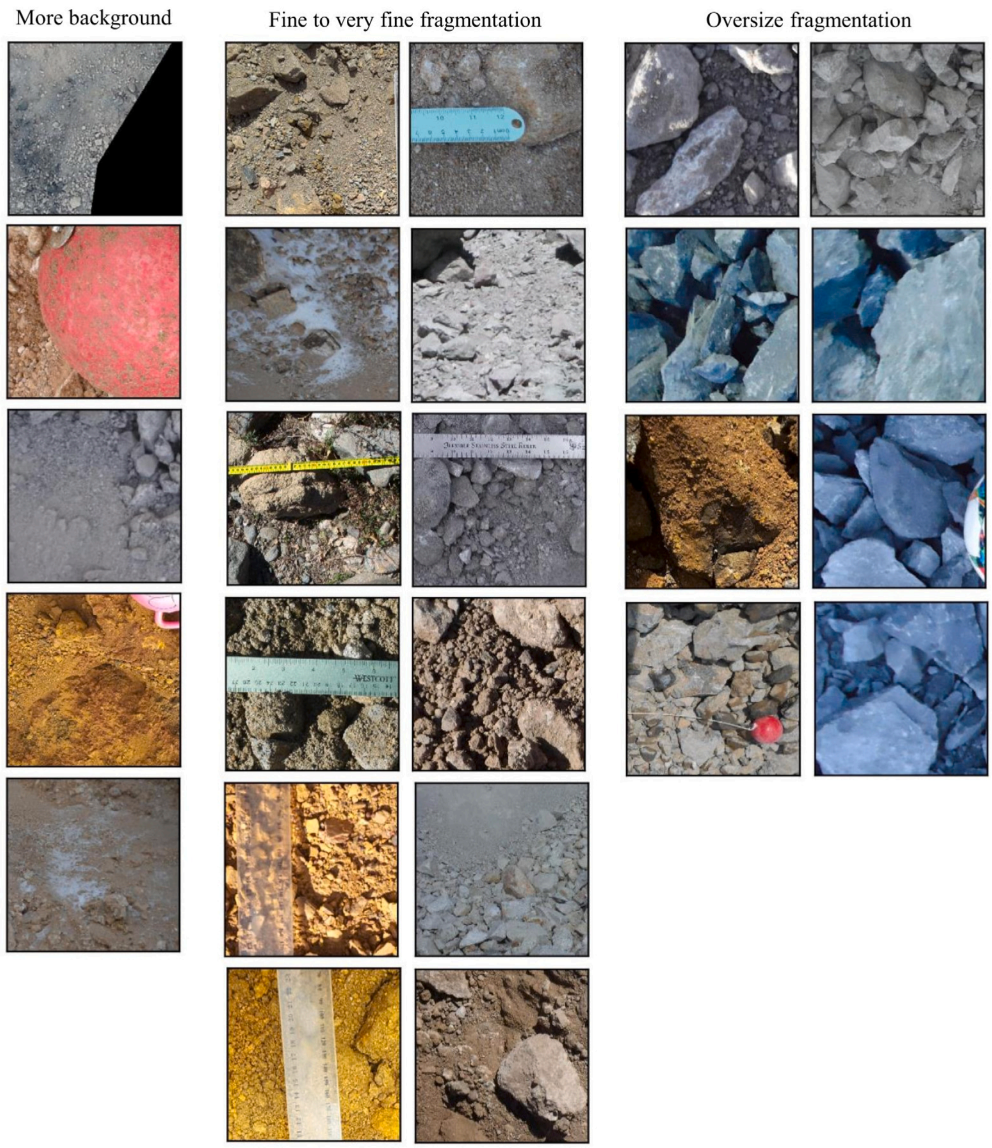

Fig. 10. Collection of sample images for the worst size analysis predictions.

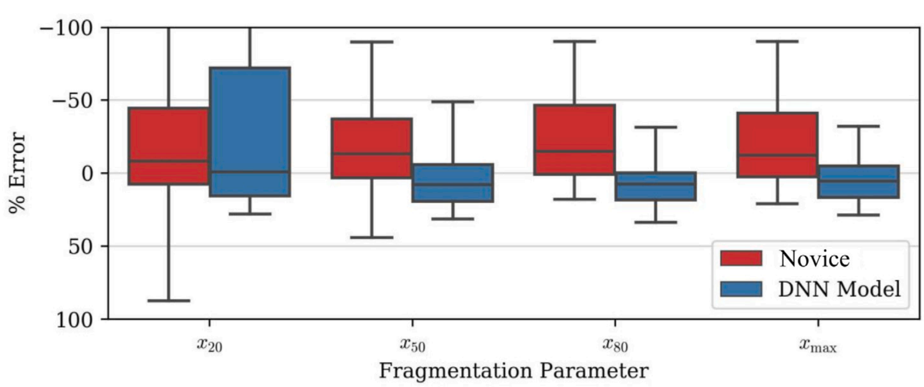

Fig. 11. Percent error box plots for each fragmentation parameter measured for Muckpile 1 by novice analysis and DNN model compared with expert manual labelling. Whiskers are at the 5% and 95% percentiles. Outliers beyond the whisker range are not plotted. (For interpretation of the references to colour in this figure legend, the reader is referred to the web version of this article.)

h by the expert. This increase in effort was caused by the decrease in GSD when compared with Muckpile 1. Patch extraction and analysis code were used to generate 97 non-overlapping image samples with their measured fragmentation parameters at a GSD of 1 cm/px. These image samples were then used as input to the DNN model to compute predicted parameters in approximately 3 s. Fig. 13 shows percent error

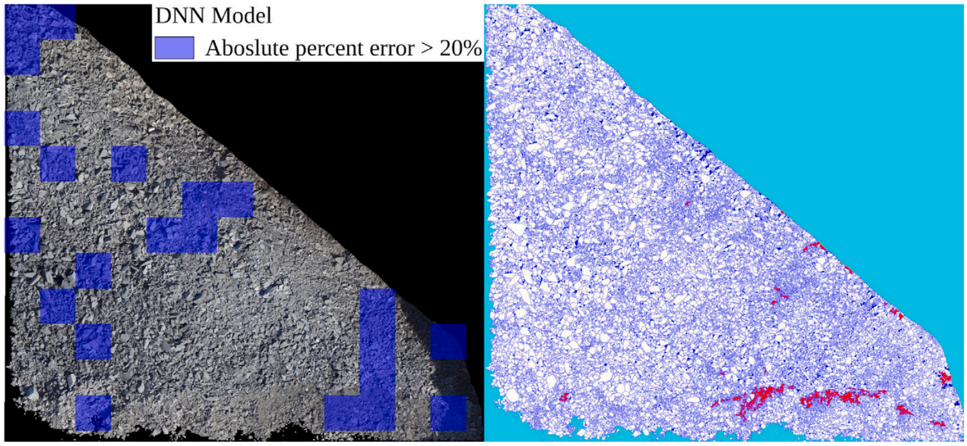

Fig. 12. Absolute percent error of x_{50} prediction for Muckpile 2 compared with manual labelling (**left**). Patches coloured blue represent an absolute percent error greater than 20%. All other patches have an absolute percent error less than 20%. Manual labelling image for Muckpile 2 (**right**). (For interpretation of the references to colour in this figure legend, the reader is referred to the web version of this article.)

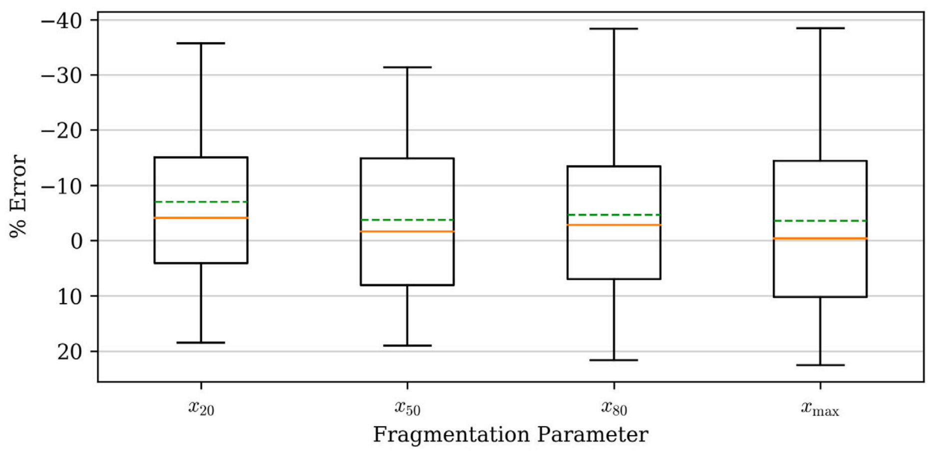

Fig. 13. Percent error box plots for each fragmentation parameter measured for Muckpile 2 by DNN model compared with expert manual labelling.

box plots for each predicted fragmentation parameter when compared with manual labelling. As the figure illustrates, the percent error for the characteristic sizes ranges from −40% to 20%, where more than 50% of the data set has a percent error of −10% to 15%. This range of error is considered acceptable because it is lower than the ranges reported for digital image analysis. To understand how the network performed for different conditions, the orthomosaic was overlain with patches for each image sample that had an absolute percent error for x_{50} greater than 20%. Fig. 12 shows Muckpile 2 overlain with these patches highlighted in blue. As can be seen in the figure, the network under performs in image samples where the edge of a large shadow forms two distinct regions and where boulders and fines regions are contained within the same sample. These results are expected because digital image analysis methods also struggle in these types of conditions. To help make the DNN model more robust to these cases, more data for these complex conditions should be collected and labelled for training the neural network.

7.2. Fragmentation size distribution

Granulation curves for rock fragments are presented in Fig. 14 for Muckpile 1 and Muckpile 2. These curves are commonly used by mine technical staff to assess blast fragmentation. To create these curves, a size distribution curve was fit to the characteristic sizes for each sample image. Using the size distribution, a granulation histogram was generated for each sample. By summing the bins of the sample image granulation histograms, an overall granulation histogram was compiled for each muckpile analysis. Then these overall granulation histograms were used to create the granulation curves shown in Fig. 14. The DNN model underprediction and novice analysis overprediction errors that have been described for Muckpile 1 in Section 7.1 are evident when inspecting these curves. The predicted granulation curve with the DNN model is closer to expert analysis than results produced by novice analysis. Even though some image samples have a large range of error, the DNN model is still able to capture the heterogeneity of fragmentation, visible throughout Muckpile 1. For Muckpile 2, the predicted granulation curve with the DNN model is even closer to the manually labelled granulation curve, where much of the size range matches the manually labelled results. These results show that DNN model predictions for Muckpile 1 and Muckpile 2 perform relatively well in comparison with the manual labelling, without requiring significant time for analysis.

When comparing all granulation curves in Fig. 14 with manual analyses generated without using patch extraction (not shown), all the curves generated using patch extraction are shifted towards finer sizes. This is thought to be caused by patch extraction because it disintegrates coarse and oversize fragments along image sample borders. This is also thought to be caused by distribution fitting which has been observed to cause the original granulation curve for each patch to narrow. To reduce this error, larger patches could be extracted or fragments that are located along patch borders can be excluded when generating data sets. Image scaling could also be implemented to reduce this

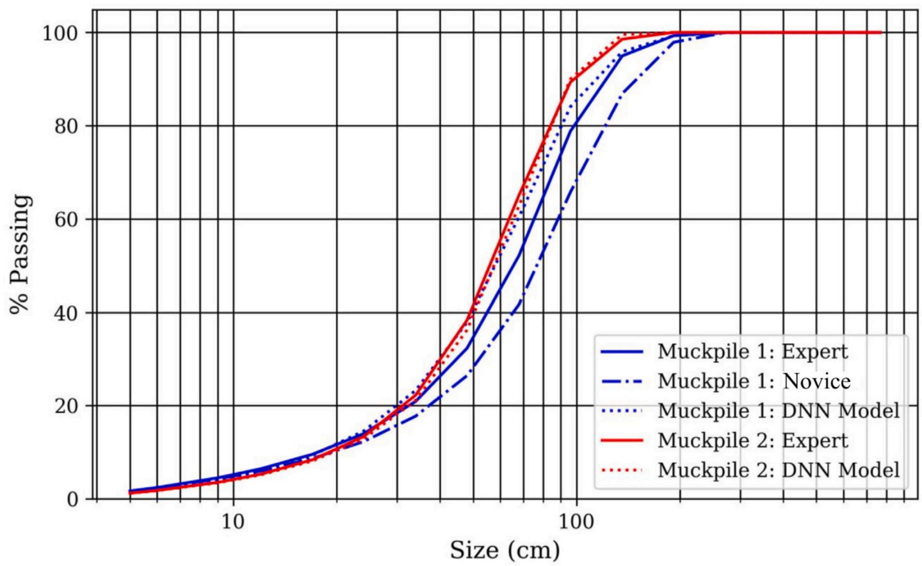

Fig. 14. Granulation curves generated for Muckpile 1 and Muckpile 2.

error for coarse fragments, similar to the zooming technique described by Santamarina et al.[34] and Schenk et al.[24] to capture fine fragments. To use this technique, a merging method needs to be developed to merge predictions made by the DNN model at different image scales.

7.3. Comparison with sieving

Sieving analysis is commonly used to determine the accuracy of fragmentation analysis methods. A sieving validation data set was used to compare sieving analysis with DNN model predictions and manual image labelling. The sieving validation data set is composed of 8 images of screened piles created using run-of-mine material in an open pit mine. These include 1 image capturing a pile with fragment sizes less than 4'' (A), 4 images of piles with fragments ranging in size from 4'' to 8'' (B-E), and 3 images of piles with sizes greater than 8'' (F-H). Fig. 15 shows 3 examples alongside their manual labelling, one for each fragment size range. These screened piles and their construction have been described in Bamford.[22] Analysis code was used to measure the fragmentation parameters determined by manual labelling. To determine the predicted parameters, the raw images were used as input to the DNN model. Once the fragmentation parameters were predicted, the GSD for each image was used to scale the parameters from pixels to inches for comparison with each image's sieving analysis.

Table 6 provides the percent of fragments within the sieved size range for each pile for manual labelling analysis and the DNN model. The percent within sieve size range varies from 60% to 100% for manual labelling, whereas the DNN model has a range from 47% to 81%. For some piles, where the fragments within the sieved range are only 47% to 74%, the amount of error is considered to be relatively high. However, it is not expected that these digital image analysis techniques will be in full agreement with sieving analysis because non-contact methods only measure the surface of the pile. The GSD used to scale the parameters could also contribute to this difference. Each pile used a central rock fragment that was also visible in an orthomosaic of the screening area to measure the GSD. This was required to determine GSD because scale objects were not available in this data set. Due to the difference in perspective of these central fragments and orthomosaic model reconstruction error, the GSD could produce significant error. For most piles (B-G) the DNN model has comparable accuracy to manual labelling. However, for very fine and very coarse examples (A and H), the DNN model did not perform at the same accuracy of manual labelling. It is thought that this decrease in performance is

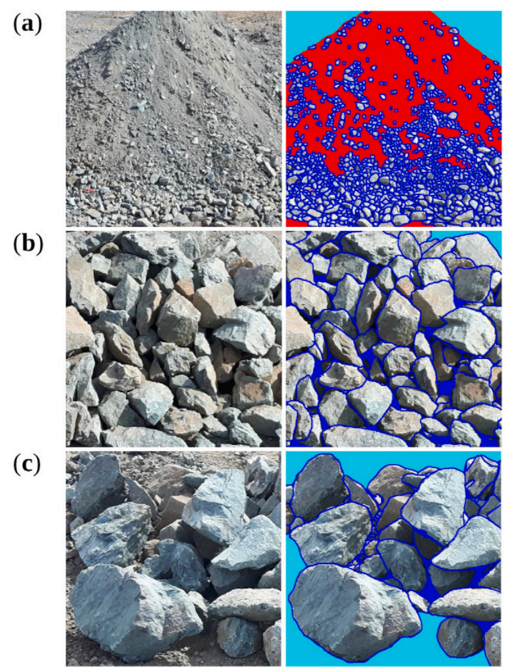

Fig. 15. Example source images (**left**) with their labelled image (**right**) from screening data set. (**a**) Fragment sizes less than 4'', (**b**) sizes ranging from 4'' to 8'' and (**c**) fragments greater than 8''.

caused by less training examples with these types of fragmentation. To help make the DNN model more robust to these cases, more data for these conditions should be collected and labelled for training the neural network.

8. Conclusion

The results of a deep neural network model for measurement of blast-induced rock fragmentation was presented in this study. The DNN model provides reasonable fragmentation measurement compared with manual labelling in significantly less time. The percent error for coarse characteristic size prediction ranges within ±25% when evaluated using the test set. With this quality of results, the DNN model only required a

Table 6
Percent within sieved range for each screened pile image for manual labelling and DNN model.

Pile	Pile description	Manual labelling	DNN model
A	Sizes less than 4"	100%	47%
B	Sizes from 4" to 8"	68%	78%
C	Sizes from 4" to 8"	74%	65%
D	Sizes from 4" to 8"	73%	70%
E	Sizes from 4" to 8"	60%	65%
F	Sizes greater than 8"	81%	80%
G	Sizes greater than 8"	77%	81%
H	Sizes greater than 8"	88%	68%

fraction of the time for analysis when compared with manual labelling. For example, for an orthomosaic with 153 image samples the DNN model only required 5 s for analysis whereas manual labelling took 11.5 h. The best measurements of characteristic size using the test set were found for images with well-defined rock boundaries and mid-range to coarse fragmentations. The worst measurements were found for images containing more background and fine to very fine or oversize fragmentation. For orthomosaic images, the worst measurements were found for samples where the edge of a large shadow forms two distinct regions and where boulders and fines regions are contained within the same sample. The results presented in this study show that the current DNN model has surpassed the accuracy of novice analysis with smaller error range and mean percent error. Even though this study's comparison with sieving shows that the DNN model was comparable with manual labelling accuracy for the majority of screened piles (6/8), more improvement is still necessary to better the prediction.

To accelerate towards this improvement, the deep learning code has been structured so that any fragmentation parameter measured by the analysis code can be used to train a neural network with any specified architecture. Once a more accurate architecture is developed, the model can be trained quickly and applied to any fragmentation parameter that blast engineers use to track blast performance. This could range from percent optical fines, oversize count, to the full granulation curve. Comparing these measurements to the blast's predicted fragmentation can be used to guide blast design optimization.

The prediction of additional fragmentation parameters and implementing fragment segmentation using DNNs is currently under investigation. Future work aims to improve the accuracy of the method for data collected by aerial methods and data collected in varying conditions. This will be done by collecting and labelling aerial data in variable lighting and rock mass conditions, such as texture, moisture, homogeneity/heterogeneity of fragmentation, etc., to create larger data sets for training. In addition, data sets from alternative perspectives, such as conveyor belt, primary crusher and shovel camera sources, will also be used to explore the deep learning approach for fragmentation measurement. More data labelling will also help to understand how much human error is present when labelling images and how well the DNN model is able to generalize.

Declaration of competing interest

The authors declare that they have no known competing financial interests or personal relationships that could have appeared to influence the work reported in this paper.

Acknowledgements

The authors would like to acknowledge the support of mining companies for conducting data collection and Split Engineering for providing labelled data.

Funding

This work was supported by the Natural Sciences and Engineering Research Council of Canada (NSERC) [grant number CRDPJ 508741-17]; and the Ontario Center of Excellence, Canada (OCE) [grant number 28271].

References

1. Stiehr JF ed, *ISEE Blasters' Handbook*. 18th ed. Cleveland, US: International Society of Explosives Engineers (ISEE); 2011.
2. Hustrulid W. *Blasting Principles for Open Pit Mining*. Rotterdam, NL: A. A. Balkema; 1999.
3. Scott A. Blastability and blast design. In: Proc. 5th Int. Symp. Rock Fragm. Blasting. Montréal, CA; 1996:163–170.
4. Kuznetsov VM. The mean diameter of fragments formed by blasting rock. *Sov. Min. Sci.*. 1973;9(2):144–148. http://dx.doi.org/10.1007/BF02506177.
5. Cunningham CVB. Fragmentation estimations and the Kuz-Ram model - Four years on. In: Proc. 2nd Int. Symp. Rock Fragm. Blasting. Keystone, US; 1987:475–487.
6. Cunningham CVB. The Kuz-Ram fragmentation model - 20 years on. In: Proc. Eur. Fed. Explos. Eng. Brighton, GB; 2005:201–210.
7. Ouchterlony F. The Swebrec function: Linking fragmentation by blasting and crushing. *Min. Technol.*. 2005;114:29–44. http://dx.doi.org/10.1179/037178405X44539.
8. Ouchterlony F, Sanchidrián JA, Moser P. Percentile fragment size predictions for blasted rock and the fragmentation-energy fan. *Rock Mech. Rock Eng.*. 2016;50:751–779. http://dx.doi.org/10.1007/s00603-016-1094-x.
9. Ouchterlony F, Sanchidrián JA. A review of development of better prediction equations for blast fragmentation. *J. Rock Mech. Geotech. Eng.*. 2019;11(5):1094–1109. http://dx.doi.org/10.1016/j.jrmge.2019.03.001.
10. Sanchidrián JA, Segarra P, Ouchterlony F, López LM. On the accuracy of fragment size measurement by image analysis in combination with some distribution functions. *Rock Mech. Rock Eng.*. 2009;42(1):95–116. http://dx.doi.org/10.1007/s00603-007-0161-8.
11. Noy MJ. Automated rock fragmentation measurement with close range digital photogrammetry. In: Sanchidrián JA, Singh AK, eds. *Measurement and Analysis of Blast Fragmentation*. London, GB: CRC Press; 2012:13–21.
12. Campbell AD, Thurley MJ. Application of laser scanning to measure fragmentation in underground mines. *Min. Technol.*. 2017;126(4):240–247. http://dx.doi.org/10.1080/14749009.2017.1296668.
13. Raina AK. A history of digital image analysis technique for blast fragmentation assessment and some Indian contributions. In: Sanchidrián JA, Singh AK, eds. *Measurement and Analysis of Blast Fragmentation*. London, GB: CRC Press; 2012:3–11.
14. Franklin JA, Katsabanis T eds, *Measurement of Blast Fragmentation: Proceedings of the Fragblast-5 Workshop on Measurement of Blast Fragmentation*. Rotterdam, NL: A. A. Balkema; 1996.
15. Sanchidrián JA, Singh AK eds, Measurement and analysis of blast fragmentation. London, GB: CRC Press; 2012.
16. Eden DJ, Franklin JA. Disintegration, fusion and edge fidelity. In: Franklin JA, Katsabanis T, eds. *Measurement of Blast Fragmentation*. Rotterdam, NL: A. A. Balkema; 1996:127–132.
17. Ramezani M, Nouranian S, Bell I, Sameti B, Tafazoli S. Fast rock segmentation using artificial intelligence to approach human-level accuracy. *J Explos Eng.* 2017;34(4):28–32.
18. Noy MJ. Evaluation of a new vision system algorithm for automated fragmentation measurement from a shovel. In: Proc. 11th Int. Symp. Rock Fragm. Blasting. Sydney, AU; 2015:721–726.
19. Thurley MJ. Automated, on-line, calibration-free, particle size measurement using 3D profile data. In: Sanchidrián JA, Singh AK, eds. *Measurement and Analysis of Blast Fragmentation*. London, GB: CRC Press; 2012:23–32.
20. Tamir R, Wagner M, Campbell J, Dakers N. Utilization of aerial drones to optimize blast and stockpile fragmentation. *J Explos Eng.* 2017;34(4):6–15.
21. Bamford T, Esmaeili K, Schoellig AP. A real-time analysis of post-blast rock fragmentation using UAV technology. *Int J Min Reclam Environ.* 2017;31(6):439–456. http://dx.doi.org/10.1080/17480930.2017.1339170.
22. Bamford T, Esmaeili K, Schoellig AP. Evaluation of UAV system accuracy for automated fragmentation measurement. In: Proc. 12th Int. Symp. Rock Fragm. Blasting. Luleå, SE; 2018:715–730.
23. Leite F, Miranda V, Palangio T. Pattern expansion optimization model based on fragmentation analysis with drone technology. In: Proc. 12th Int. Symp. Rock Fragm. Blasting. Luleå, SE; 2018:731–740.
24. Schenk F, Tscharf A, Mayer G, Fraundorfer F. Automatic muck pile characterization from UAV images. *ISPRS Ann Photogramm Remote Sens Spat Inf Sci.* 2019;IV-2/W5:163–170. http://dx.doi.org/10.5194/isprs-annals-IV-2-W5-163-2019.
25. He K, Ghioxari G, Dollár P, Girshick R. Mask R-CNN. 2017. https://arxiv.org/abs/1703.06870.

26. Lin T, Maire M, Belongie S, Bourdev L, Girshick R, Hays J, Perona P, Ramanan D, Zitnick CL, Dollár P. Microsoft COCO: Common objects in context. 2014. https://arxiv.org/abs/1405.0312.
27. Split Engineering LLC. Split-desktop software. 2019. https://www.spliteng.com/products/split-desktop-software.
28. Cunningham CVB. Keynote address: Optical fragmentation assessment - A technical challenge. In: Franklin JA, Katsabanis T, eds. *Measurement of Blast Fragmentation*. Rotterdam, NL: A. A. Balkema; 1996:13–19.
29. Maerz NH, Palangio TC, Franklin JA. WipFrag image based granulometry system. In: Franklin JA, Katsabanis T, eds. *Measurement of Blast Fragmentation*. Rotterdam, NL: A. A. Balkema; 1996:91–99.
30. He K, Zhang X, Ren S, Sun J. Deep residual learning for image recognition. 2015. https://arxiv.org/abs/1512.03385.
31. LeCun Y, Bengio Y, Hinton G. Deep learning. *Nature*. 2015;521:436–444. http://dx.doi.org/10.1038/nature14539.
32. Kingma DP, Ba J. Adam: A method for stochastic optimization. In: Proc. 3rd Int. Conf. Learn. Represent. San Diego, US; 2015:1–15.
33. Chollet F, et al. Keras. 2015. https://keras.io.
34. Santamarina JC, Franklin JA, Morley M, Wang DS. Development and testing of a zooming technique for fragmentation measurement. In: Franklin JA, Katsabanis T, eds. *Measurement of Blast Fragmentation*. Rotterdam, NL: A. A. Balkema; 1996:133–139.